Scripta Materialia 209 (2022) 114359

Contents lists available at ScienceDirect

Scripta Materialia

journal homepage: www.elsevier.com/locate/scriptamat

Nanomechanical and microstructural characterization on the synergetic strengthening in selectively laser melted austenitic stainless steel

Dong-Hyun Lee[a,*], Zhe Gao[b], Jeong-Min Park[b], Yakai Zhao[c], Jin-Yoo Suh[d,*], Eric A. Jägle[e], Koichi Tsuchiya[f], Upadrasta Ramamurty[c,g], Jae-il Jang[b,*]

[a] Department of Materials Science and Engineering, Chungnam National University, Daejeon 34134, Republic of Korea
[b] Division of Materials Science and Engineering, Hanyang University, Seoul 04763, Republic of Korea
[c] School of Mechanical and Aerospace Engineering, Nanyang Technological University, Singapore 639798, Republic of Singapore
[d] Center for Energy Materials Research, Korea Institute of Science and Technology, Seoul 02792, Republic of Korea
[e] Institute of Materials Science, Universität der Bundeswehr München, 85579 Neubiberg, Germany
[f] Research Center for Structural Materials, National Institute for Materials Science (NIMS), Tsukuba, Ibaraki 305-0047, Japan
[g] Institute of Materials Research Engineering, Agency for Science, Technology and Research, Singapore 138634, Republic of Singapore

ARTICLE INFO

Article history:
Received 18 August 2021
Revised 3 October 2021
Accepted 18 October 2021
Available online 30 October 2021

Keywords:
Additive manufacturing
Austenitic stainless steel
High-pressure torsion
Nanoindentation
Martensitic transformation

ABSTRACT

The significant strengthening of selectively laser melted (SLM) 304L stainless steel that occurs due to high-pressure torsion (HPT) is examined by recourse to detailed nanomechanical and microstructural characterization. In the as-built alloy, dislocation hardening is the main strengthening mechanism. After HPT, however, the synergistic combination grain refinement and martensitic transformation dominate the strength of the alloy. In the nanocrystalline regime, the dominance of the grain boundary-mediated plasticity retards the martensite-induced hardening.

Additive manufacturing (AM) of metallic materials has evolved impressively in the recent past and is now deployed in a variety of industries. However, many scientific, technological, and economic challenges for its wider application still remain [1–6]. One of the major scientific challenges is the development of detailed microstructure-mechanical property relations, since the AM alloys often exhibit complex microstructures with nm to mm scale hierarchy such as solidification cells with elemental segregation and nanoscale precipitation along their boundaries, refined grains with strong textures, and mesostructures that reflect the hatch spacing, layer thickness, and scan rotations [1–6]. In this context, AM austenitic stainless steels, mostly prepared by selective laser melting (SLM), are especially attractive because their hierarchical features lead to not only the excellent strength-ductility combination but also other interesting properties including toughness and hydrogen embrittlement resistance [7–12].

In the present paper, the possibility of further tailoring such complex microstructures for enhancing the mechanical performance, through severe plastic deformation (SPD) route, is explored. It was reported that high-pressure torsion (HPT) process, one of the representative SPD techniques [13–16], indeed led to a remarkable increase in hardness of SLM 316L austenitic stainless steel [17–19], due mainly to the grain refinement. Keeping this in mind, we examine the different strengthening mechanisms and the interplay between them in HPT SLM 304L steel.

The 304L stainless steel blocks with dimension of 60 × 30 × 9 mm^3 were fabricated using a commercial SLM (also often called laser powder bed fusion, L-PBF) machine (Aconity Mini, Aconity 3D GmbH, Germany). During the process, layer thickness, laser power, hatch spacing, and scan speed were set at 30 μm, 180 W, 80 μm, and 700 mm/s, respectively. The scanning direction was rotated by 90° after each layer. The as-built SLM sample (denoted as "SLM" sample) was machined into disks (with 10 mm diameter and ~0.8 mm thickness) from the plane perpendicular to the build direction. They were HPT processed for 0.25, 0.5, 1, and 2 turns under a pressure of 5.0 GPa at 1 rpm. Hereafter, the SLM sample subjected to HPT will be referred to as SLM+HPT*N*, where *N* is the number of

* Corresponding authors.
E-mail addresses: dhlee@cnu.ac.kr (D.-H. Lee), jinyoo@kist.re.kr (J.-Y. Suh), jijang@hanyang.ac.kr (J.-i. Jang).

https://doi.org/10.1016/j.scriptamat.2021.114359
1359-6462/

the HPT revolutions. Vickers hardness measurements on each disk were conducted with a peak load (P_{max}) of 980 mN.

Microstructural analyses were performed by using X-ray diffraction (XRD; D/Max-2500, Rigaku-Denki, Japan) and scanning electron microscopy (SEM; Merlin compact, Carl Zeiss AG, Germany) that was accompanied with electron channeling contrast imaging (ECCI) and electron backscattered diffraction (EBSD; DigiView, EDAX-TSL, USA). For SEM, the samples were final-polished using VibroMet 2 polisher (Buehler, USA) with 0.02 μm colloidal silica. Transmission electron microscopy (TEM; Tecnai F20, Thermo Fisher Scientific, USA) with ASTAR (NanoMEGAS, Belgium) was performed on the samples prepared by focused ion beam (FIB; Helios NanoLab 600, Thermo Fisher Scientific, USA) milling. Nanoindentation tests were conducted using the Nanoindenter-XP (KLA Corporation, USA) equipped with both Berkovich and cube-corner tips with a P_{max} of 100 mN; indentation strain rate was maintained 0.025 /s and the hold time at P_{max} was 1 s.

Both EBSD and ECCI were employed to characterize the microstructural evolution of SLM 304L steel during HPT process. Representative microstructures of the SLM sample and the edges of SLM+HPT0.25 and SLM+HPT2 disks are shown in Fig. 1. A single-phase austenitic microstructure (with the average grain size, d, of ~22 μm) containing the solidification cellular structure (with an average cell size of ~350 nm) inside each grain is seen in the SLM sample (Fig. 1a). The orientation and phase maps for SLM+HPT0.25 and SLM+HPT2 samples (Figs. 1b and 1c, respectively) were obtained through ASTAR-TEM technique considering the extreme grain refinement in them. The crucial feature in these images is the phase transformation of the FCC γ-austenite into HCP ε- and BCC α'-martensite during HPT (either $\gamma \rightarrow \alpha'$ directly or $\gamma \rightarrow \varepsilon \rightarrow \alpha'$ sequentially [20–23]). These phases were confirmed by the TEM selected area electron diffraction patterns obtained from the SLM+HPT2 sample (Fig. 1d). With increasing N (from 0.25 to 2), the fractions of ε and α' increase at the expense of γ (see Table 1). An overlay of the orientation and image quality maps (left of Figs. 1b and 1c) reveals the reduction in "overall" grain size (by assuming a single phase) to ~142 and ~62 nm for SLM+HPT0.25

Table 1
Volume fraction of each constituent phase measured by EBSD (for SLM sample) and ASTAR-TEM (for SLM+HPT samples). The average grain sizes (measured by assuming single phase) are also displayed as "overall size".

Phase	SLM	SLM+HPT0.25	SLM+HPT2
γ	100 % (~22 μm)	~25 % (~62 nm)	~7 % (~36 nm)
ε	-	~13 % (~72 nm)	~16 % (~62 nm)
α'	-	~62 % (~189 nm)	~77 % (~60 nm)
Overall size	~22 μm	~142 nm	~62 nm

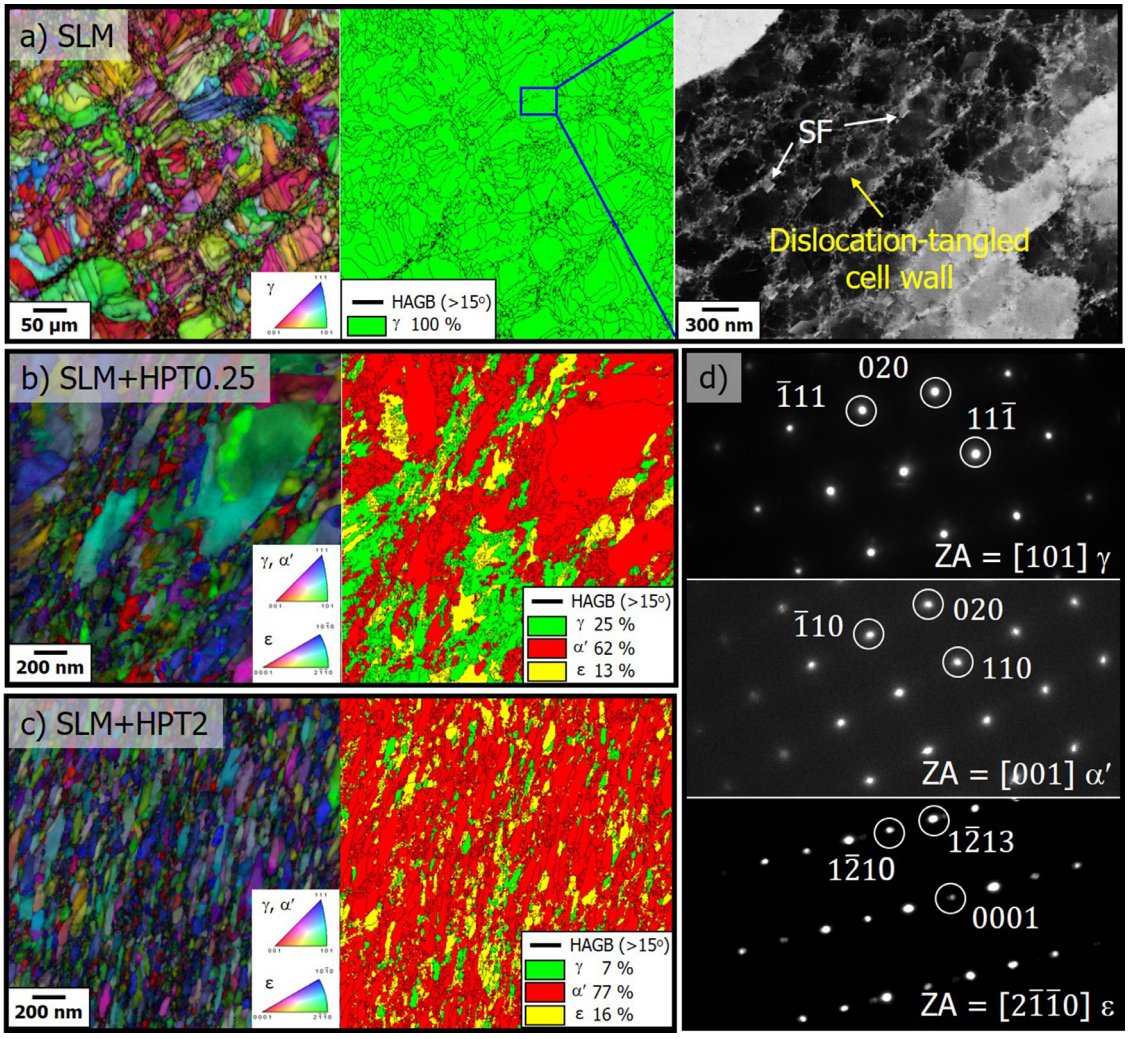

Fig. 1. Microstructural evolution during HPT processing: EBSD orientation and phase maps of the (a) SLM (also showing ECCI image), (b) SLM+HPT0.25, and (c) SLM+HPT2 samples. (d) shows the representative examples (for SLM+HPT2) of TEM selected area diffraction patterns of the constituent phases in SLM+HPT samples. Note that EBSD images were taken on the plane perpendicular to the building direction.

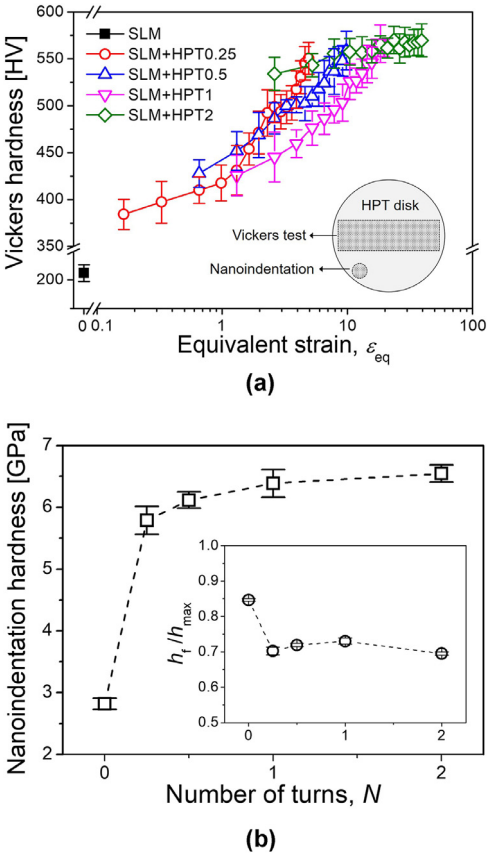

Fig. 2. (a) Variations in Vickers hardness as a function of applied equivalent strain. (Note that the *x* axis is in log scale.) Inset shows the indentation locations. (b) Changes in nanoindentation hardness and indentation plasticity with the number of turns.

and SLM+HPT2, respectively (Table 1). The HPT process also leads to a marked reduction in d of γ from ~22 μm (SLM) to ~36 nm (SLM+HPT2).

The equivalent von Mises strain, ε_{eq}, imposed on the disk during HPT can be estimated using the relation [24]: $\varepsilon_{eq} = \frac{2\pi Nr}{\sqrt{3}t}$, where r and t are the radius and thickness of the disk, respectively. The evolution in Vickers hardness as a function of ε_{eq} is shown in Fig. 2a where the hardness of SLM sample is also included at $\varepsilon_{eq} = 0$. A substantial enhancement in the hardness after merely a quarter turn of the HPT ($N = 0.25$), which eventually saturated at ε_{eq} of ~20 that approximately corresponds to the edge part of SLM+HPT1 disk, can be seen. Fig. 2b summarizes the results of the nanoindentation experiments performed with the Berkovich tip. Their values confirm the same trends as Vickers hardness. The inset of Fig. 2b displays the variation in h_f/h_{max} (where h_f is the final indentation displacement after unloading and h_{max} is the maximum displacement at P_{max}) with N. Note that h_f/h_{max} is a measure of the relative portion of the plastic deformation in the total elasto-plastic deformation that takes place during indentation [25]. Thus, hardness vs. h_f/h_{max} relation in indentation tests can be considered as a proxy to the strength vs. ductility relation in the uniaxial tensile tests. In Fig. 2b, it is evident that despite the reduction in h_f/h_{max} due to the HPT process, its values for SLM+HPT samples are still reasonably high (~0.7), implying that the observed hardening was not achieved at the expense of the significant ductility loss.

Fig. 3 displays the representative SEM and enlarged ECCI images of indentation impressions. To amplify the changes in indentation-induced plasticity, a sharper cube-corner indenter was also utilized as it can produce significantly high stresses and strains underneath the indenter [26,27]. A large number of slip steps are observed around the hardness impression made on the SLM sample (Fig. 3a). They characterize the FCC alloy deforming via planar slip [28,29]. A high density of stacking faults around the impression is also

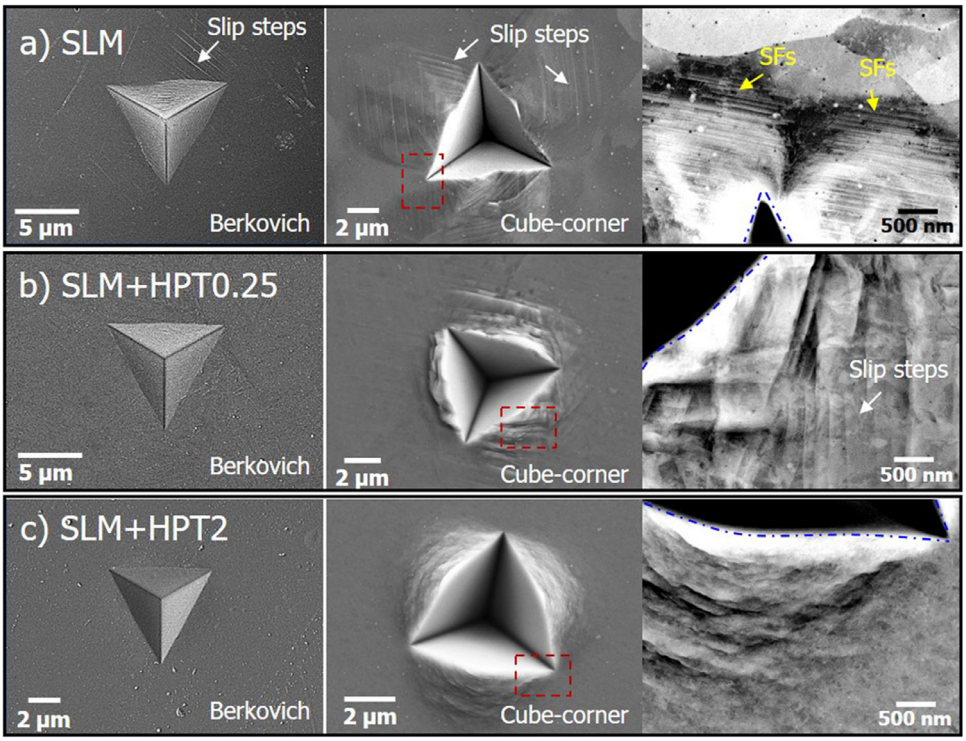

Fig. 3. Representative SEM images of the hardness impressions produced by Berkovich (left) and cube-corner indentations (middle), and zoom-in ECCI images of the region marked around the cube-corner indentation (right); (a) SLM, (b) SLM+HPT0.25, and (c) SLM+HPT2 samples. Blue dashed line in the ECCI images indicates the boundary of the hardness impression.

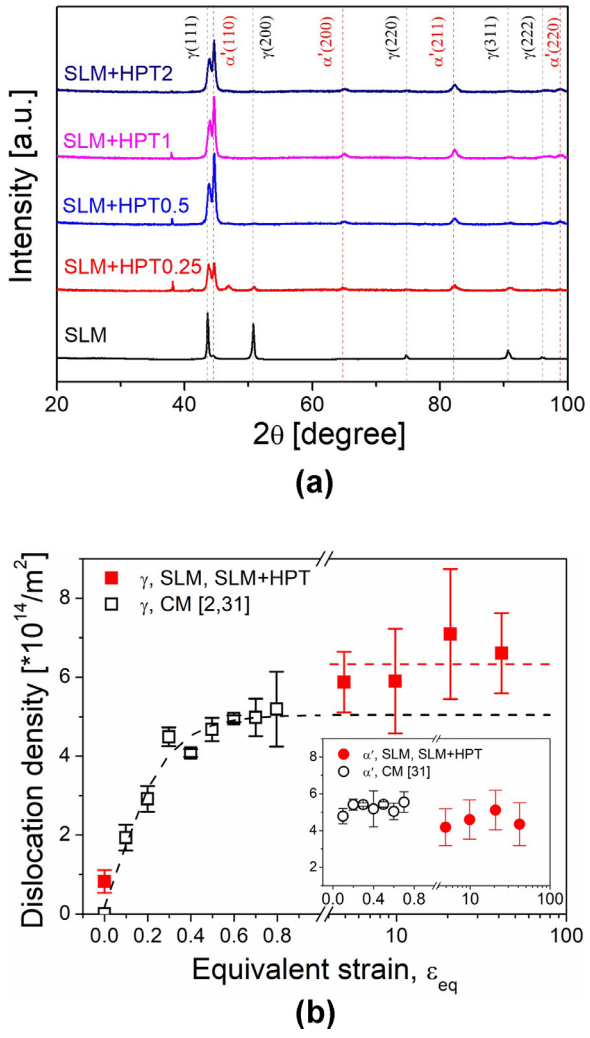

Fig. 4. X-ray diffreaction analysis of SLM and SLM+HPT samples: (a) X-ray diffraction patterns; (b) the variations in the estimated dislocation density as a function of equivalent strain.

evident from the ECCI image. It suggests the glide of partial dislocations, i.e., successive planar slip, as the predominant deformation mechanism. The slip planarity is less pronounced in SLM+HPT0.25 and SLM+HPT2 samples (Figs. 3b and 3c) with the shear offsets dominating the deformation morphology around the indented impression. Such offsets are often considered as the traces of shear bands [30]. Magnified ECCI images of them reveal that dislocation activity is gradually reduced with increasing N, as several sets of slip steps are still evident in SLM+HPT0.25 but not in SLM+HPT2.

Fig. 4a shows representative XRD scans obtained from the SLM sample and the edges of all SLM+HPT disks, which reconfirms the HPT-induced martensitic transformation. The dislocation density, ρ, was estimated from the full width at half maximum (FWHM) of the XRD line profiles by using the modified Williamson-Hall method (with aid of the modified Warren-Averbach method), as illustrated in Fig. 4b. The details of the procedure can be found elsewhere [31,32]. The peak intensity of ε is negligible and hence not considered here. For comparison, literature values of ρ for the conventionally manufactured (CM) stainless steels are also displayed in Fig. 4b. In the case of CM steels [2,31], ρ in γ (ρ_γ) increases moderately to ~5.04×10^{14} m^{-2} with increasing ε_{eq}. Ungár *et al.* [33] suggested that the relationship between ρ and ε_{eq} can be expressed as: $\rho(\varepsilon_{eq}) = [\rho_s^{1/2} - C_1 \exp(-C_2\varepsilon_{eq})]^2$, where C_1 and C_2 are material constants, and ρ_s is the saturated ρ value for the plastic deformation. The ρ_γ data for the CM steels (open squares) fit well to this equation as shown as the black dashed curve. From the fitted curve, ρ_γ for the CM steels is expected to reach ρ_s (~5.04×10^{14} m^{-2}) at ε_{eq} ~0.8. On the other hand, ρ_γ in the SLM sample (before HPT, i.e. $\varepsilon_{eq} = 0$) is determined as ~8.34×10^{13} m^{-2}, which is much higher than ~10^9–10^{10} m^{-2} observed in the annealed CM steel [2], but close to the reported value for SLM steels [18]. Upon HPT processing, ρ_γ rapidly increases to ~5.87×10^{14} m^{-2} at ε_{eq} of ~4.9 (corresponding to the edge part of SLM+HPT0.25 disk), and thereafter remains constant until the maximum applied ε_{eq} (~42). In contrast, the dislocation density in α' ($\rho_{\alpha'}$), shown in the inset of Fig. 4b, remains almost constant in the range of 4×10^{14}–5×10^{14} m^{-2} irrespective of the imposed ε_{eq} for both CM steel and SLM+HPT samples. From these observations, one can conclude that the evolution of ρ_γ in SLM sample is already saturated at 0.25 turn of HPT with a higher ρ_s (~6.33×10^{14} m^{-2}) than that of the CM steel (~5.04×10^{14} m^{-2}).

To understand the significance of grain boundary (GB) strengthening, the Hall-Petch (H-P) relationship ($\sigma_y = \sigma_0 + k_{HP}d^{-1/2}$ where σ_y and σ_0 are the yield and intrinsic stress, respectively, and k_{HP} is the H-P coefficient) is plotted in Fig. 5a where the literature data for the CM steels [34–38] are also included. The σ_y values here are estimated using the Tabor's relation [39]: $\sigma_y \sim H_M/3$, where H_M is Meyer's hardness (i.e., peak load divided by the projected area) converted from the Vickers hardness [40]. For the CM steels with only γ (open circles in Fig. 5a), σ_y values are in reasonable agreement with the H-P relation from which σ_0 and k_{HP} are determined as 408 MPa and 326 MPa·(μm)$^{1/2}$, respectively. This k_{HP} is in reasonable agreement with those reported for various austenitic steels (~253–300 MPa(μm)$^{1/2}$ [8,41,42]). It is evident in Fig. 5a that σ_y of the steels consisting $\gamma + \alpha'$ or $\gamma + \varepsilon + \alpha'$are substantially higher than those in the H-P plot for the only γ steels. This implies that the formation of harder martensite phases, α' and ε, can play an additional role in HPT-induced strengthening of the steels. It is also noteworthy in Fig. 5a that all the three σ_y of SLM, SLM+HPT0.25, and SLM+HPT2 samples are higher than those of CM steels with a similar d. This observation indicates that the strength enhancement in SLM sample (primarily due to the cellular structure [8,10,11]) is retained even after the significant grain refinement and martensitic transformation.

Since SLM sample shows much higher ρ than CM steel (Fig. 4b), the σ_y increment due to the ρ increase, $\Delta\sigma_\rho$, was calculated using the Taylor's hardening relation [43]: $\Delta\sigma_\rho = M\alpha_1 Gb(\sqrt{\rho_2} - \sqrt{\rho_1})$, where M is Taylor factor (~3.05 [41]), α_1 is an empirical constant (~0.3 [42]), G is shear modulus (~77 GPa [41]), b is the magnitude of the Burgers vector (~0.25 nm [41]), ρ_1 and ρ_2 are the ρ of the CM steel and SLM sample for a given d, respectively, e.g. see Fig. 4b. The estimated value of $\Delta\sigma_\rho$ for the SLM sample, ~169 MPa, is in good agreement with the difference in σ_y between SLM sample and CM steel for a similar d (Fig. 5a). This reaffirms that the predominant mechanism of the strength increase in SLM sample vis-à-vis CM steel is dislocation hardening, as suggested earlier [44]. For SLM+HPT0.25 and SLM+HPT2 samples, $\Delta\sigma_\rho$ in γ phase is estimated as ~48 MPa by using the saturation values of ρ_γ in Fig. 4b in the Taylor equation. Note that the SLM+HPT samples contain only small amounts of γ (Figs. 1b and 1c) and thus the actual $\Delta\sigma_\rho$ in γ are negligibly small in the samples. In addition, $\Delta\sigma_\rho$ in α' phase may also be negligible since the SLM and CM steels exhibit similar dislocation densities in α' irrespective of ε_{eq} (see the inset of Fig. 4b). Therefore, the major strengthening mechanism for SLM sample compared to CM steel (for a given d) is dislocation hardening, but not for the SLM+HPT samples.

An important question then arises is "why does SLM+HPT sample have a higher σ_y than CM steels (for a given d)?" A possible explanation is related to a larger amount of strain-induced martensites in the SLM+HPT samples. Since the cell walls (and low-angle

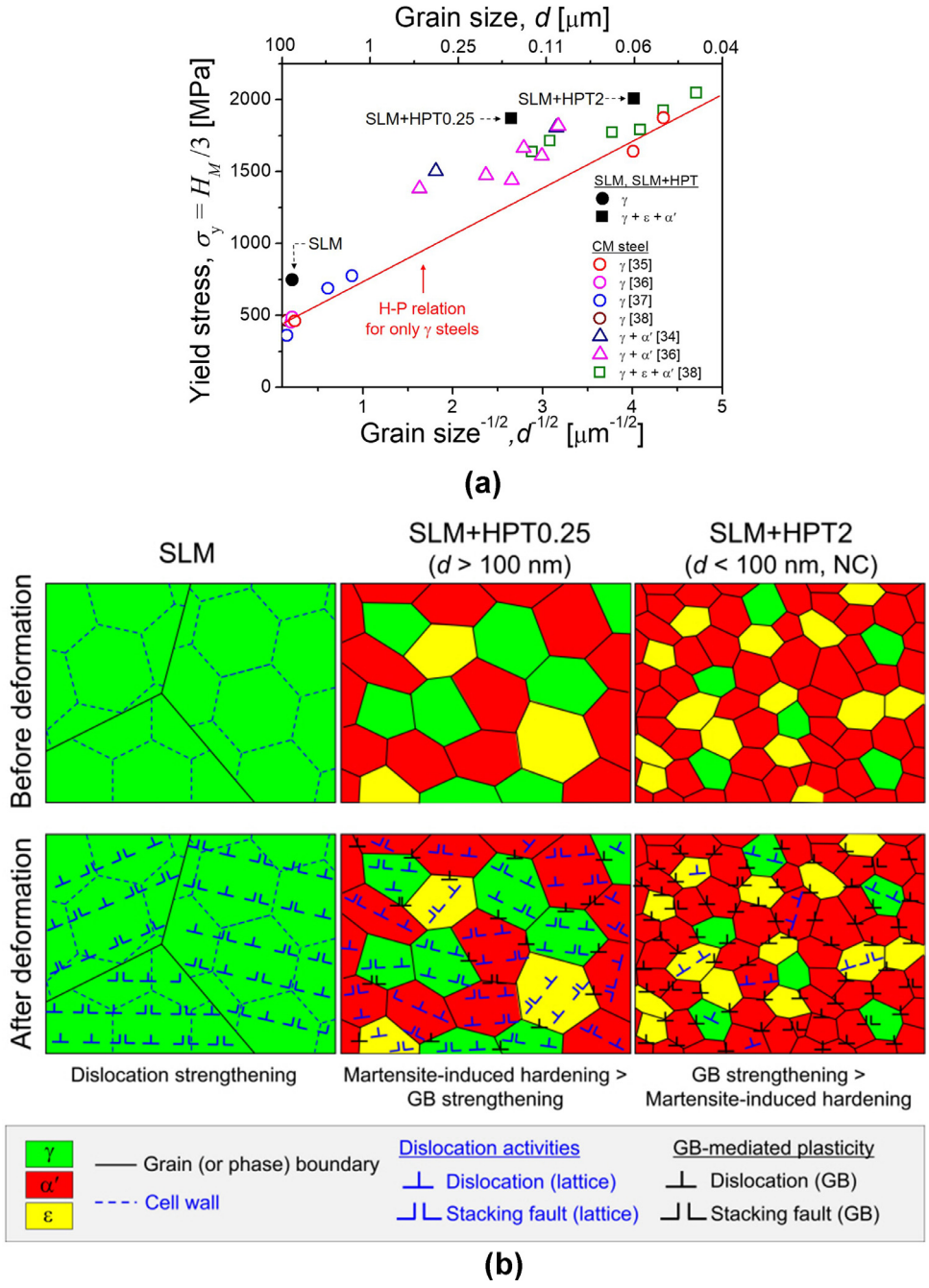

Fig. 5. (a) Hall-Petch plot for the relationship between the yield stress, σ_y, and the grain size, d, measured in this study and in earlier reports for CM steels. The steels consisting only γ, $\gamma + \alpha'$, and $\gamma + \varepsilon + \alpha'$ are denoted as symbols of circle, triangle, and square, respectively. Note that for the steels having multiple phases, d was measured by assuming a unified single phase. (b) Schematic illustration showing the change in microstucture (before and after deformation) with increasing HPT turns. Note that only deformation-induced dislocations (i.e. fresh dislocations) are displayed.

GBs) can act as nucleation sites for martensite [19], the martensitic transformation during HPT may be promoted in SLM sample. Since the volume fraction of martensites in the CM steels of Fig. 5a is unavailable in literature [34–36,38], the precise role of cellular structure in the transformation could not be provided here, but desirable to be investigated in future.

Another important feature revealed by Fig. 5a is that, in the NC regime ($d < 100$ nm), σ_y values of the steels containing both ε and α' (open squares) appear to closely follow the H-P plot drawn for the only-γ steels. This indicates that the contribution of martensitic transformation to σ_y may be less significant in the NC regime. This phenomenon might be closely related to the fact that the formation of shear bands becomes more pronounced as d is reduced to the NC regime, i.e., SLM+HPT2. Since such band formation in NC metals is often associated with the grain rotation and GB sliding [45–49], it may be construed that the predominant deformation mechanism transforms from conventional dislocation activity in the SLM sample to GB-mediated plasticity in the SLM+HPT2 sample. To verify such a possibility, the value of activation volume, V^*, was estimated by performing a series of nanoindentation at various indentation strain rates. As shown in Fig. S1 of Supplementary Information, the value of V^* decreases from $\sim 15b^3$ to $\sim 5b^3$ upon HPT processing. Considering that GB-mediated plasticity corresponds to a low V^* ($< 10b^3$) [50–52], the current results imply

that GB-mediated plasticity indeed becomes predominant in the SLM+HPT samples. On this basis, the degradation of martensite-induced strengthening in NC regime can be explained, as following (schematically illustrated in Fig. 5b). For $d > 100$ nm, while a large extent of dislocation activity is still available within the grains, the contribution of the martensitic transformation to strengthening is non-negligible due to the relatively higher lattice friction stress in the martensite (as compared to that in the austenite). Plastic deformation in NC regime is not governed by dislocation glide through lattice, but by GB-mediated plasticity, and hence grain refinement has a more dominant effect on σ_y than martensite transformation. This mechanism also rationalizes the fact that the difference in σ_y between SLM+HPT samples and CM steels for a given d (which may be due to a larger amount of martensite in the former) decreases with increasing N from 0.25 to 2 (Fig. 5a).

In summary, significant HPT-induced strengthening of the SLM 304L steel was achieved by the synergy among dislocation multiplication, grain refinement, and martensitic transformation. GB-mediated plasticity becomes predominant and hence martensite-induced strengthening becomes negligible in the NC regime, suggesting that there is a certain HPT strain level up to which the synergistic effect can be maximized. For the present steel, it would be $\varepsilon_{eq} \sim 4.9$. This offers us a direction for tailoring SLM steel's microstructure for achieving high strength without promoting GB-mediated plasticity that can introduce localized deformation and/or creep deformation.

Declaration of Competing Interest

The authors declare that they have no known competing financial interests or personal relationships that could have appeared to influence the work reported in this paper.

Acknowledgements

The work at Chungnam National University was supported by the National Research Foundation of Korea (NRF) grants funded by the Korea government (MSIT) (No. 2021R1F1A1048393). The work at Hanyang University was supported by the NRF grants (No. 2020R1A2B5B01001446 and No. 2020R1A5A6017701). The work at Nanyang Technological University was supported by Agency for Science, Technology and Research (A*STAR) of Singapore via the Structural Metal Alloys Programme (No. A18B1b0061). The work at Universität der Bundeswehr München was supported by Deutsche Forschungsgemeinschaft (DFG) in the framework of the priority program "SPP 2006" (No. JA 2482/3-2). The work at NIMS was supported by a Grant-in-Aid for Scientific Research on Innovative Area, "High-Entropy Alloys-Science of New Class of Materials Based on Elemental Multiplicity and Heterogeneity" through MEXT, Japan (No. 18H05451). We thank Mr. Cheol-Hwee Shim at KIST for the ASTAR-TEM operation.

Supplementary materials

Supplementary material associated with this article can be found, in the online version, at doi:10.1016/j.scriptamat.2021.114359.

References

[1] D. Herzog, V. Seyda, E. Wycisk, C. Emmelmann, Acta Mater 117 (2016) 371–392.
[2] S. Gorsse, C. Hutchinson, M. Gouné, R. Banerjee, Sci. Technol. Adv. Mater. 18 (2017) 584–610.
[3] T. DebRoy, T. Mukherjee, J.O. Milewski, J.W. Elmer, B. Ribic, J.J. Blecher, W. Zhang, Nat. Mater. 18 (2019) 1026–1032.
[4] D. Gu, X. Shi, R. Poprawe, D.L. Bourell, R. Setchi, J. Zhu, Science 372 (2021) eabg1487 80-.)..
[5] D.R. Feenstra, R. Banerjee, H.L. Fraser, A. Huang, A. Molotnikov, N. Birbilis, Curr. Opin. Solid State Mater. Sci. 25 (2021) 100924.
[6] D. Lee, Y. Zhao, S.Y. Lee, D. Ponge, E.A. Jägle, Scr. Mater. 207 (2022) 114308.
[7] T. Voisin, J.-B. Forien, A. Perron, S. Aubry, N. Bertin, A. Samanta, A. Baker, Y.M. Wang, Acta Mater 203 (2021) 116476.
[8] Y.M. Wang, T. Voisin, J.T. McKeown, J. Ye, N.P. Calta, Z. Li, Z. Zeng, Y. Zhang, W. Chen, T.T. Roehling, R.T. Ott, M.K. Santala, P.J. Depond, M.J. Matthews, A.V. Hamza, T. Zhu, Nat. Mater. 17 (2018) 63–71.
[9] T. Pinomaa, M. Lindroos, M. Walbrühl, N. Provatas, A. Laukkanen, Acta Mater 184 (2020) 1–16.
[10] D.-H. Lee, B. Sun, S. Lee, D. Ponge, E.A. Jägle, D. Raabe, Mater. Sci. Eng. A 803 (2021) 140499.
[11] J.-M. Park, Y. Zhao, T. Voisin, D.-H. Lee, S. Komazaki, Y. Ko, D.-I. Kim, J.-Y. Suh, H.N. Han, Y.M. Wang, U. Ramamurty, J. Jang, Scr. Mater. 194 (2021) 113718.
[12] P. Kumar, Z. Zhu, S.M.L. Nai, R.L. Narayan, U. Ramamurty, Scr. Mater. 202 (2021) 114002.
[13] A.P. Zhilyaev, T.G. Langdon, Prog. Mater. Sci. 53 (2008) 893–979.
[14] D.-H. Lee, I.-C. Choi, M.-Y. Seok, J. He, Z. Lu, J.-Y. Suh, M. Kawasaki, T.G. Langdon, J. Jang, J. Mater. Res. 30 (2015) 2804–2815.
[15] D.-H. Lee, M.-Y. Seok, Y. Zhao, I.-C. Choi, J. He, Z. Lu, J.-Y. Suh, U. Ramamurty, M. Kawasaki, T.G. Langdon, J. Jang, Acta Mater 109 (2016) 314–322.
[16] I.-C. Choi, J. Jang, Adv. Eng. Mater. 22 (2020) 1900648.
[17] S. Mohd Yusuf, M. Nie, Y. Chen, S. Yang, N. Gao, J. Alloys Compd. 763 (2018) 360–375.
[18] S. Mohd Yusuf, Y. Chen, S. Yang, N. Gao, Mater. Charact. 159 (2020) 110012.
[19] A. Heidarzadeh, M. Neikter, N. Enikeev, L. Cui, F. Forouzan, R.T. Mousavian, Mater. Sci. Eng. A 811 (2021) 141086.
[20] G.B. Olson, M. Cohen, J. Less-Common Met. 28 (1972) 107–118.
[21] K. Spencer, M. Véron, K. Yu-Zhang, J.D. Embury, Mater. Sci. Technol. 25 (2009) 7–17.
[22] T. Masumura, N. Nakada, T. Tsuchiyama, S. Takaki, T. Koyano, K. Adachi, Acta Mater 84 (2015) 330–338.
[23] Y. Tian, A. Borgenstam, P. Hedström, J. Alloys Compd. 766 (2018) 131–139.
[24] R.Z. Valiev, Y.V. Ivanisenko, E.F. Rauch, B. Baudelet, Acta Mater 44 (1996) 4705–4712.
[25] Y. Zhao, J.-M. Park, D.-H. Lee, E.J. Song, J.-Y. Suh, U. Ramamurty, J. Jang, Scr. Mater. 168 (2019) 76–80.
[26] J. Jang, G.M. Pharr, Acta Mater 56 (2008) 4458–4469.
[27] D.-H. Lee, J.-A. Lee, M.-Y. Seok, U.B. Baek, S.H. Nahm, J. Jang, Int. J. Hydrogen Energy 39 (2014) 1897–1902.
[28] K.A. Nibur, D.F. Bahr, Scr. Mater. 49 (2003) 1055–1060.
[29] Y. Zhao, D.-H. Lee, M.-Y. Seok, J.-A. Lee, M.P. Phaniraj, J.-Y. Suh, H.-Y. Ha, J.-Y. Kim, U. Ramamurty, J. Jang, Scr. Mater. 135 (2017) 54–58.
[30] J.R. Trelewicz, C.A. Schuh, Acta Mater 55 (2007) 5948–5958.
[31] T. Shintani, Y. Murata, Acta Mater 59 (2011) 4314–4322.
[32] F. HajyAkbary, J. Sietsma, A.J. Böttger, M.J. Santofimia, Mater. Sci. Eng. A 639 (2015) 208–218.
[33] T. Ungár, L. Li, G. Tichy, W. Pantleon, H. Choo, P.K. Liaw, Scr. Mater. 64 (2011) 876–879.
[34] İ. Üçok, T. Ando, N.J. Grant, Mater. Sci. Eng. A 133 (1991) 284–287.
[35] H. Wang, I. Shuro, M. Umemoto, K. Ho-Hung, Y. Todaka, Mater. Sci. Eng. A 556 (2012) 906–910.
[36] A. Belyakov, M. Odnobokova, A. Kipelova, K. Tsuzaki, R. Kaibyshev, IOP Conf. Ser. Mater. Sci. Eng. 63 (2014) 012156.
[37] G. Marnier, C. Keller, J. Noudem, E. Hug, Mater. Des. 63 (2014) 633–640.
[38] J. Gubicza, M. El-Tahawy, Y. Huang, H. Choi, H. Choe, J.L. Lábár, T.G. Langdon, Mater. Sci. Eng. A 657 (2016) 215–223.
[39] D. Tabor, The Hardness of Metals, Clarendon Press, 1951.
[40] J. Jang, S. Shim, S. Komazaki, T. Honda, J. Mater. Res. 22 (2007) 175–185.
[41] M. Karavaeva, M. Abramova, N. Enikeev, G. Raab, R. Valiev, Metals (Basel) 6 (2016) 310.
[42] J.G. Kim, N.A. Enikeev, J.B. Seol, M.M. Abramova, M.V. Karavaeva, R.Z. Valiev, C.G. Park, H.S. Kim, Sci. Rep. 8 (2018) 11200.
[43] Y. Estrin, H. Mecking, Acta Metall 32 (1984) 57–70.
[44] Z. Li, B. He, Q. Guo, Scr. Mater. 177 (2020) 17–21.
[45] D. Jia, K.T. Ramesh, E. Ma, Acta Mater 51 (2003) 3495–3509.
[46] J.T.M. De Hosson, W.A. Soer, A.M. Minor, Z. Shan, E.A. Stach, S.A. Syed Asif, O.L. Warren, J. Mater. Sci. 41 (2006) 7704–7719.
[47] M. Dao, L. Lu, R. Asaro, J.T.M. De Hosson, E. Ma, Acta Mater 55 (2007) 4041–4065.
[48] I. Sabirov, Y. Estrin, M.R. Barnett, I. Timokhina, P.D. Hodgson, Acta Mater 56 (2008) 2223–2230.
[49] F. Liang, B. Zhang, Y. Yong, X.-M. Luo, G.-P. Zhang, Int. J. Plast. 132 (2020) 102745.
[50] H. Conrad, Mater. Sci. Eng. A 341 (2003) 216–228.
[51] Y. WANG, A. HAMZA, E. MA, Acta Mater. 54 (2006) 2715–2726.
[52] H. Conrad, Nanotechnology 18 (2007) 325701.